Scholte wave inversion and passive source imaging with ocean-bottom DAS

Ethan F. Williams[1], María R. Fernández-Ruiz[2], Regina Magalhaes[2], Roel Vanthillo[3], Zhongwen Zhan[1], Miguel González-Herráez[2], and Hugo F. Martins[4]

https://doi.org/10.1190/tle40080576.1

Abstract

Geotechnical characterization of marine sediments remains an outstanding challenge for offshore energy development, including foundation design and site selection of wind turbines and offshore platforms. We demonstrate that passive distributed acoustic sensing (DAS) surveys offer a new solution for shallow offshore geotechnical investigation where seafloor power or communications cables with fiber-optic links are available. We analyze Scholte waves recorded by DAS on a 42 km power cable in the Belgian offshore area of the southern North Sea. Ambient noise crosscorrelations converge acceptably with just over one hour of data, permitting multimodal Scholte wave dispersion measurement and shear-wave velocity inversion along the cable. We identify anomalous off-axis Scholte wave arrivals in noise crosscorrelations at high frequencies. Using a simple passive source imaging approach, we associate these arrivals with individual wind turbines, which suggests they are generated by structural vibrations. While many technological barriers must be overcome before ocean-bottom DAS can be applied to global seismic monitoring in the deep oceans, high-frequency passive surveys for high-resolution geotechnical characterization and monitoring in coastal regions are easily achievable today.

Introduction

With the growth of both conventional and renewable offshore energy production, high-resolution and low-cost methods for geotechnical characterization of submarine sediments are of increasing significance for site selection, design, and monitoring of marine structures, pipelines, and cables. Of particular significance is the shear-wave velocity profile of shallow sediments. Shear-wave velocity parameters such as V_{S30} and $Z_{1.0}$ are commonly used in ground motion prediction equations, which are a primary tool in estimating both probabilistic seismic and liquefaction hazard (e.g., Abrahamson and Silva, 2008). Shear modulus or shear-wave velocity is also used as a proxy for site properties such as the small-strain stiffness and large-strain strength of sediments (Seed and Idriss, 1970; Shi and Asimaki, 2017). In combination with measurements of compressional wave velocity or bulk modulus, shear-wave velocities are sensitive to the pore fluid saturation, pore fluid composition, and porosity of sediments (Berryman et al., 2002). Time-dependent changes in the shear-wave velocity of shallow sediments may be utilized to monitor compaction and deformation patterns associated with oil and/or gas production (Hatchell et al., 2009).

Most conventional approaches to onshore seismic site characterization, however, are challenging or even impossible to apply offshore because the water column is opaque to shear waves. For example, the popular multichannel analysis of surface waves (MASW) method (Park et al., 1999) can be accomplished on land by a small crew using only a hammer or weight-drop source and standard geophone array. Conversely, underwater MASW utilizing converted Scholte waves requires a towed source such as an air gun, along with an array of ocean-bottom hydrophones or seismometers (Bohlen et al., 2004; Park et al., 2005). On land, the advent of ambient noise interferometry for surface wave tomography has revolutionized seismic site characterization by eliminating the need for an active source, permitting noninvasive passive investigations using surface waves generated by distant ocean–solid earth interactions (microseism) or local human activities such as vehicle traffic (Shapiro et al., 2005). Offshore studies with ambient noise Scholte waves have shown significant potential in creating highly repeatable maps of near-surface velocity structure (de Ridder and Dellinger, 2011; de Ridder and Biondi, 2013; Mordret et al., 2013). However, the trade-off between cost and resolution in ocean-bottom seismometry limits the potential of conventional instrumentation for high-resolution, shallow studies. Where preexisting seafloor fiber-optic cables are available, such as at offshore wind farms, distributed acoustic sensing (DAS) offers a viable alternative to ocean-bottom seismometers because deployment cost does not scale with the number of sensors.

DAS arrays leveraging preexisting fiber-optic cables have shown tremendous potential for near-surface geophysics and infrastructure monitoring onshore (Zhan, 2020). The particular sensitivity of DAS to longitudinal waves renders it well-suited to surface wave studies, which have been employed widely in seismic site characterization and shear-wave velocity inversion (Dou et al., 2017; Spica et al., 2020b). Further, the ability of DAS to record strain signals across a broad frequency band has permitted such diverse applications as pipeline integrity monitoring (Tanimola and Hill, 2009), urban traffic monitoring (Wang et al., 2020), active-source seismic imaging (Mateeva et al., 2013), and earthquake detection (Jousset et al., 2017; Lindsey et al., 2017; Li and Zhan, 2018). Recently, three concurrent studies by Lindsey et al. (2019), Sladen et al. (2019), and Williams et al. (2019) demonstrated that DAS can have similar value when deployed on seafloor fiber-optic cables, recording local, regional, and teleseismic earthquakes along with ambient noise Scholte waves generated by ocean–solid earth interaction. Subsequently, Spica et al. (2020a)

[1]California Institute of Technology, Seismological Laboratory, Pasadena, California, USA. E-mail: efwillia@caltech.edu; zwzhan@caltech.edu.
[2]University of Alcala, Polytechnic School, Department of Electronics, Alcala de Henares, Spain. E-mail: rosario.fernandezr@uah.es; regina.magalhaes@uah.es; miguel.gonzalezh@uah.es.
[3]Marlinks, Leuven, Belgium. E-mail: roel.vanthillo@marlinks.com.
[4]Instituto de Optica, Madrid, Spain. E-mail: hugo.martins@csic.es.

and Cheng et al. (2021) demonstrated that Scholte waves in ocean-bottom DAS data can be utilized for structural investigations, and Zhan et al. (2020) and Karrenbach et al. (2020) showed that ocean-bottom DAS can record active source shots with fidelity similar to ocean-bottom seismometers.

In this article, we demonstrate the utility of DAS for offshore engineering applications by analyzing one hour of passive DAS data from an ocean-bottom cable offshore from Belgium. Between 0.3 and 5 Hz, the data set is dominated by Scholte waves propagating along the sediment–water interface. We measure multimode Scholte wave dispersion from ambient noise correlations and invert for a shallow shear-wave velocity model along the cable. We then investigate anomalous Scholte wave phases present in the noise correlations that interfere with the direct wave between virtual source and receiver. By migrating these off-axis Scholte waves, we find they originate from individual wind turbines operating near the cable.

Data overview

We analyze a one-hour passive DAS recording from an optical fiber within a 42 km power cable servicing wind farms in the southern North Sea, offshore from Zeebrugge, Belgium. Figure 1 shows the path of the cable relative to local bathymetry and offshore wind farms. The water depth is less than 40 m along the entire cable, which crosses several sand ridges. Most notable is Thornton Bank, which has hosted the 54-turbine C-Power wind farm since 2009. The burial depth of the cable varies between 0.5 and 3.5 m below the seafloor. While nine separate wind farm projects are active or under construction on both sides of the Belgium–Netherlands maritime boundary, only three were fully commissioned (C-Power, Northwind, and Belwind/Nobelwind) and one was partially commissioned (Rentel) at the time of data acquisition on 19 August 2018 (Figure 1).

The fiber was interrogated using a chirped-pulse DAS system built by the University of Alcala (Pastor-Graells et al., 2016). A major advantage of chirped-pulse DAS is its use of direct detection, as opposed to coherent detection used in conventional DAS systems, which eliminates fading sensitivity along the fiber (Fernandez-Ruiz et al., 2018), permitting array processing directly from the raw data. For the interested reader, extended reviews of this technique outlining the instrumental details are available (Fernandez-Ruiz et al., 2019). The channel spacing was set at 10 m, with 10 m gauge length and 10 Hz sampling rate (downsampled from a 1 kHz original sampling rate), yielding 4192 channels of continuous data over the full 42 km range of the cable. The DAS recorded ambient noise Scholte waves generated by ocean–solid earth interactions and anthropogenic sources. This data set also includes a teleseismic earthquake. While some Scholte wave conversions from teleseismic P- and S-phases may be present, we were unable to identify earthquake-related Scholte waves and assume they do not contribute to the results presented here. For more details about the data set, choice of interrogator, and cable design, we refer the reader to Williams et al. (2019).

Phase velocity measurement and inversion

To compute ambient noise correlation functions, the one-hour DAS record was divided into 3.4-minute windows (2048 samples at 10 Hz) overlapping by 50%. The first 1000 channels near shore and in the surf zone were discarded. Spectral whitening was applied to each window, followed by crosscorrelation, normalization, and stacking in the frequency domain. Scholte wave dispersion images were computed by applying the τ–p transform on a 100-channel (1 km) virtual source gather every 10 channels (100 m) along the array, yielding 309 dispersion images (Figures 2a and 2b). Initial phase velocity picks were chosen automatically as the maximum value of the dispersion image in each frequency bin and then reviewed manually to assign mode numbers and remove spurious picks.

Scholte wave phase velocity picks for the fundamental mode and first overtone were jointly inverted for a 1D local shear-wave velocity profile, fixing density at 1600 g/cc (Figures 2c and 2d). For simplicity, we use a power-law parameterization ($c(z) = c_0 z^{\nu}$) for which an approximate analytical Scholte wave dispersion solution is given by Godin and Chapman (Chapman and Godin, 2001; Godin and Chapman, 2001). A power-law velocity model is convenient because it permits straightforward calculation of common geotechnical quantities such as V_{S30} — the time-averaged shear-wave velocity of the top 30 m, $c_0(1-\nu)30^{\nu}$ — and $Z_{1.0}$ — the depth to 1 km/s shear-wave velocity, $\left(1000/c_0\right)^{1/\nu}$ — without having to consider the shallow resolution of a layered model or apply nonphysical regularization to the inversion. Theoretical and experimental studies have demonstrated that unconsolidated marine sediments typically exhibit power-law shear-wave velocity in the top tens of meters due to the steep gradient in confining pressure below the seafloor (Hamilton, 1976; Bryan and Stoll, 1988; Godin and Chapman, 1999; Buckingham, 2005). While this assumption may not apply for regions of the cable where unconsolidated Quaternary sediments are thin, consolidated/cemented sediments

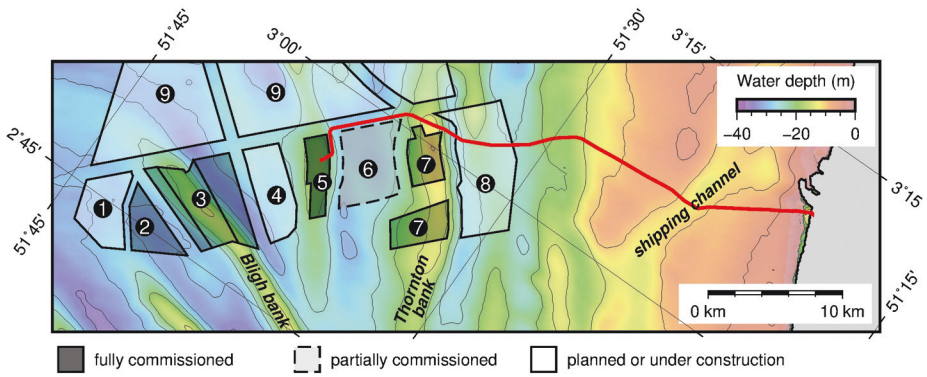

Figure 1. Map of seafloor power cable (red line) and wind farms (boxes) offshore Belgium. Labeled wind farms are color coded by degree of completion at the time of data acquisition in August 2018 and are as follows: (1) Mermaid, (2) Northwester, (3) Belwind/Nobelwind, (4) Seastar, (5) Northwind, (6) Rentel, (7) C-Power, (8) Norther, and (9) Borssele.

also exhibit nonlinear dependence of shear-wave velocity on confining pressure (e.g., Christensen and Wang, 1985), and power-law or piecewise power-law models are frequently used to represent shallow consolidated sediments in ground-motion studies (Boore and Joyner, 1997; Brocher, 2008). Further, choice of a power-law velocity model is supported by the data, as phase velocity is observed to scale as a power of frequency (Figure 2b; Godin and Chapman, 2001; Tsai and Atiganyanun, 2014). The inversion was carried out with the Metropolis-Hastings algorithm, with convergence determined by the effective sample size. The marginal posterior probability density functions for c_0 and ν are approximately Gaussian but exhibit multiple local maxima due to the high scatter among dispersion picks at low frequencies (Figure 2c). Consequently, we consider the mean of the posterior as the solution, instead of the maximum a posteriori point (Figure 2d).

The inverted velocity profile and associated geotechnical parameters are shown in Figure 3. All along the cable, uncertainty decreases with water depth. Because only one hour of data is available, the signal-to-noise ratio of Scholte waves is a limiting factor in dispersion measurement, and in shallow water ocean surface gravity wave signals dominate the data, inhibiting convergence of noise correlation functions and resulting in more scattered dispersion picks. High uncertainty between 32 and 34 km may also result from the rough bathymetry of numerous short-wavelength sand dunes on the crest of Thornton Bank. Localized extreme (greater than 50% V_{S30}) high-velocity anomalies at 10–11 km and 39–40 km are likely a result of bends in the cable (Figure 1).

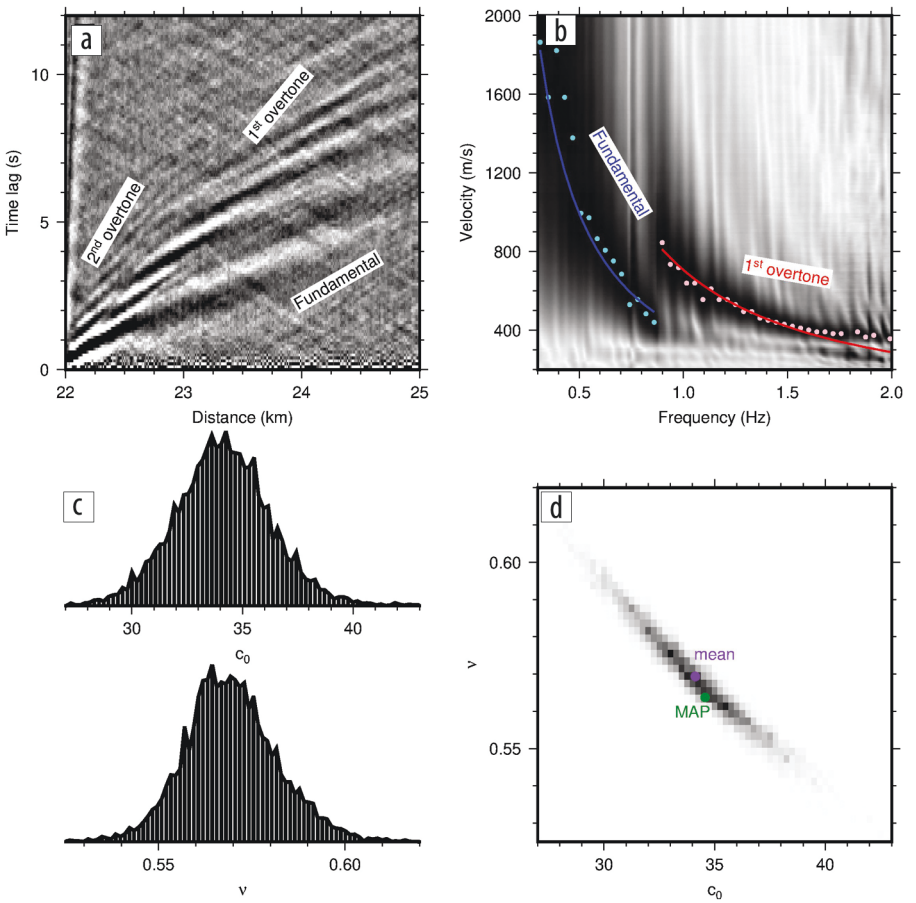

Figure 2. Scholte wave dispersion measurement and inversion. (a) Common-source gather with virtual source at 22 km, showing three Scholte wave modes and a weak ocean surface gravity wave mode (near vertical, along the *y*-axis) propagating along the array. (b) Normalized dispersion image computed with the τ–p transform. Dispersion picks for the fundamental mode (blue) and first overtone (red) are shown with the mean posterior fit. (c) Marginal posterior probability density functions (PDFs) for the two parameters c_0 and ν. (d) Joint posterior PDF of c_0 and ν, with the mean point and maximum a posteriori (MAP) point labeled.

The resulting shear-wave velocity model is generally consistent with known geologic information, despite the inability of a power-law model to capture discrete interfaces. The shallow stratigraphy of the Belgian Continental Shelf is characterized by Eocene shelf deposits unconformably overlain by Quaternary sands, which form a series of tidal sand banks. Between 10 and 20 km cable distance, the thickness of Quaternary deposits decreases from approximately 15 m to less than 5 m, while the composition of Eocene strata (clay to clayey sandstone) remains similar (Le Bot et al., 2005; Mathys, 2009). The thinning of unconsolidated Quaternary sands is consistent with the observed decreasing trend in V_{S30} over this interval (Figure 3d). Several strong anomalies in V_{S30} and $Z_{1.0}$ between 10 and 20 km may be associated with early Quaternary channels incising the top-Paleoene unconformity, such as have been mapped by Mathys (2009) in multichannel seismic profiles near the cable path. A small anomaly in both V_{S30} and $Z_{1.0}$ at 22 km is likely associated with a local increase in the thickness of the Quaternary sand. Minimal velocity change is evident at Thornton Bank; rather, significant (20%–40%) high-V_{S30} anomalies are observed in the swales on either side of the bank, correlated with the deepest bathymetry at 29 and 36 km (Figures 3d and 3e). Here, the Quaternary deposits are thinnest (less than 5 m), and in places erosion from tidal currents may expose the Eocene at the seafloor (Le Bot et al., 2005; Mathys, 2009). The velocity model also reveals an increase in $Z_{1.0}$ across the last 15 km of the cable, from approximately 400 to 450 m, with a step around 32 km under the western flank of Thornton Bank (Figure 3e). An increase in $Z_{1.0}$ while the background trend in V_{S30} remains constant indicates a decrease in the gradient of shear-wave velocity with depth. While this could be explained by the changes in sand thickness at Thornton Bank, the cable also crosses several boundaries in the Eocene section grading from clay to sandstone in the last 15 km (Le Bot et al., 2005), so interpretation of this trend is complex.

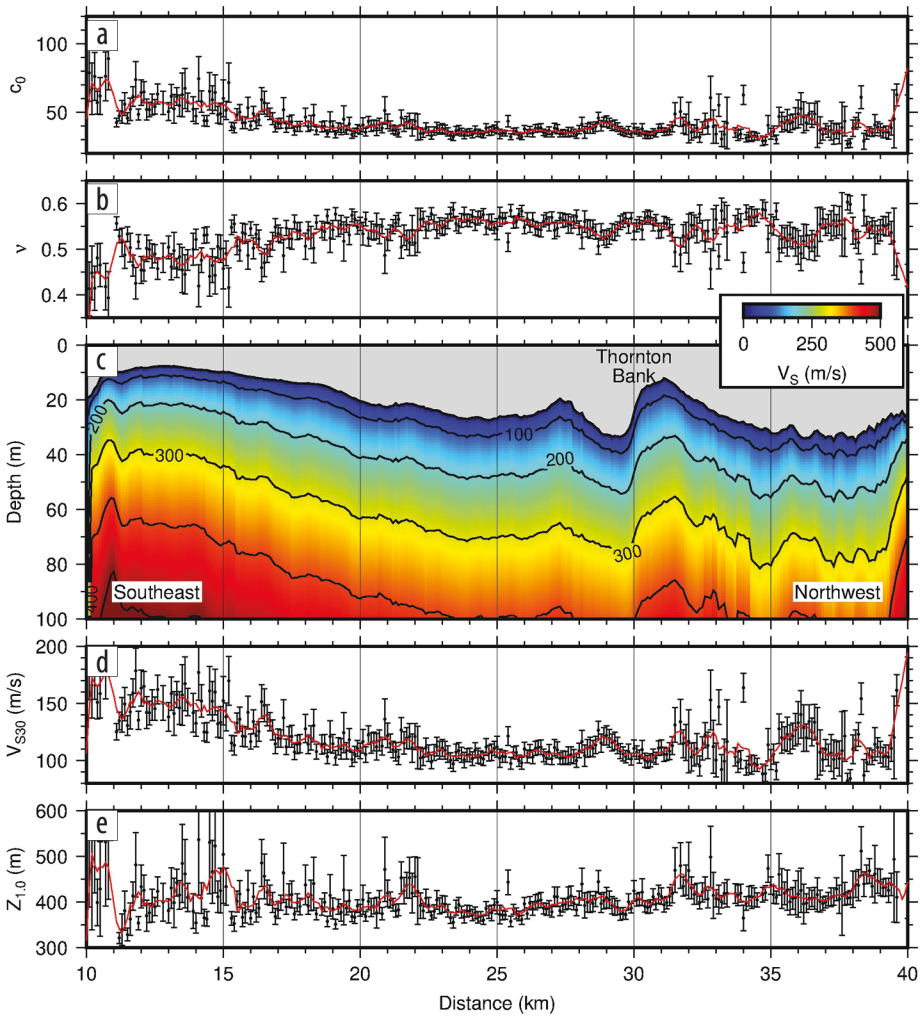

Figure 3. Velocity model. (a) and (b) Inversion results for c_0 and ν along the 30 km array segment from southeast to northwest, showing the mean posterior solution (black dot), one standard deviation (black bar), and a the mean solution smoothed with a 500 m spatial window (red line). (c) Smoothed velocity model (same as smoothed red line in [a] and [b]) offset by bathymetry. Panels (d) and (e) are the same as (a) and (b) but for geotechnical parameters V_{S30} and $Z_{1.0}$.

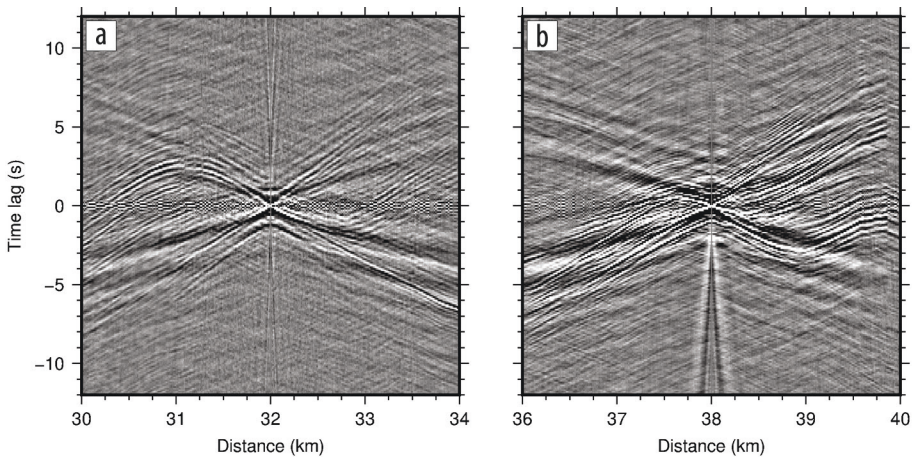

Figure 4. Common-source gathers with virtual sources at (a) 32 km and (b) 38 km showing interference between the direct Scholte wave arrivals and strong secondary sources along the cable. Compare with Figure 2a where no off-axis arrivals are present.

Interferometric imaging of noise sources

In addition to the expected direct Scholte wave modes propagating between virtual source and receiver (Figure 2a), noise correlation virtual source gathers also exhibit hyperbolae indicative of obliquely incident Scholte waves generated by a strong secondary source or scatterer (Figure 4). These off-axis arrivals interfere with the second and third overtones of the direct wave in dispersion images, requiring us to exclude all picks above 2 Hz from the shear-wave velocity inversion above. Similar arrivals were observed by Mordret et al. (2013) in noise correlations across a dense ocean-bottom node array at Valhall, where the source was localized to the drilling platform by beamforming and traveltime fitting. Precursory and coda phases from secondary sources and scatterers are relatively common features of continental-scale noise correlations (e.g., Zhan et al., 2010; Ma et al., 2013) and have also been observed in high-frequency noise correlations on terrestrial DAS arrays (Zeng et al., 2017). Given these off-axis arrivals only appear between 30 and 42 km distance where the cable runs along the northern edge of the C-Power, Rentel, and Northwind wind farms, we infer that off-axis arrivals in noise correlation functions represent Scholte waves generated by the structural vibrations of wind turbines. This interpretation is validated by passive source imaging.

To visualize the secondary noise sources and prepare for migration, we sort the noise correlations into common-offset gathers (Figure 5). In common-offset gathers, the traveltime curve for an off-axis point source or scatterer appears similar to an arc-tangent curve, with zero crossing at the point where the source is an equal distance from both virtual source and virtual receiver (i.e., located along a line perpendicular to the array), permitting straightforward visual identification of source locations and minimizing the overlap between each source. Conveniently, the traveltime of the direct wave between virtual source and virtual receiver is approximately constant in common-offset

gathers (Figure 5a), so the direct wave is effectively removed by subtracting the mean trace from all midpoints (Figure 5b). Residual common-mode noise (generated by temperature or vibrations of the DAS interrogator unit) that was not completely removed before crosscorrelation concentrates at zero time lag in the crosscorrelation functions and is also mitigated by removing the mean at this stage.

Scholte waves from at least five secondary noise sources are clearly present in the data — one centered around 31 km, a second at 35 km, and at least three more around 38 km. These arrivals are only visible between 1 and 4 Hz and have a strong spectral peak around 1.1 Hz that varies slightly among sources. The narrow-band source signature combined with the dispersive nature of Scholte waves results in ringy waveforms almost 4 s long. By using the envelope, the effect of dispersion can be neglected during migration.

To compute the source image, we migrated individual common-offset gathers using the crosscorrelation migration of Schuster et al. (2004), which is simply Kirchhoff migration reformulated for interferometric traveltimes. Because the amplitude of observed Scholte waves varies by an order of magnitude among sources, we divided the data into three continuous segments and migrate each independently: 29.5–32.5 km, 32.5–36.5 km, and 36.5–41.5 km. Because we are migrating the envelope and because we have no information about velocity away from the cable, we used a constant velocity, taken as the average group velocity for the fundamental mode between 1 and 4 Hz, which is between 100 and 120 m/s along the array.

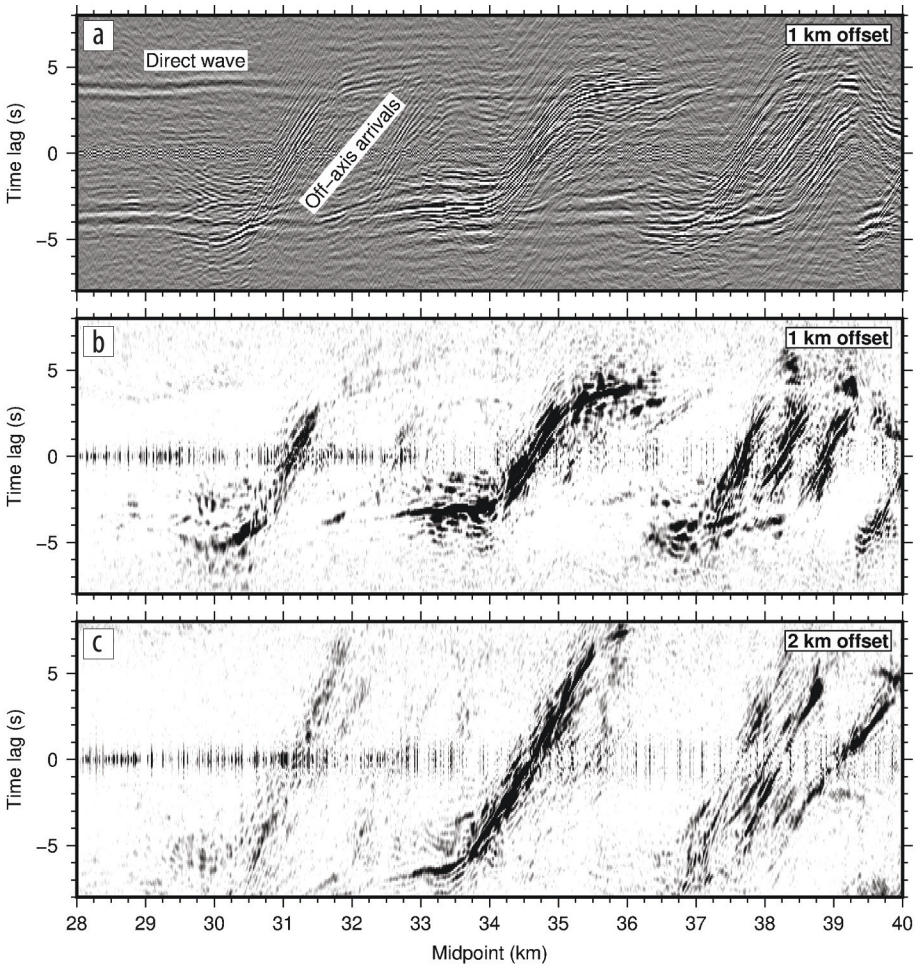

Figure 5. (a) Common-offset gather (h = 500 m) showing three areas of strong off-axis Scholte wave arrivals around 31, 35, and 38 km. (b) Common-offset gather from (a) after filtering 1–4 Hz, calculating the envelope, and removing the mean. Panel (c) is the same as (b) but with h = 1 km.

Resulting source images are shown in Figure 6. For the first two cable segments, the off-axis arrivals migrate clearly to a single turbine source: turbine I3 in the C-Power wind farm (Figure 6b) and turbine E4 in the Rentel wind farm (Figure 6c). The smearing of energy along the direction perpendicular to the cable is caused by the linear and one-sided array configuration. For the third cable segment (Figure 6d), interpretation of the source image is more ambiguous. Two strong peaks appear at turbines F1 and F2 with two weaker peaks at turbines G1 and G2, due to crossing of traveltime curves around the bend in the DAS array. There is also broad smearing of energy across turbine rows C through E farther from the array, which is caused by the overlap of the Scholte waves from each of the sources at longer time lags. Though operational ground truth is not available from the wind farm operators, at the time of acquisition the Rentel wind farm was still under construction and not fully commissioned until November 2018, which likely explains why only a subset of turbines is observed. No turbines in the Northwind wind farm are clearly identified, though this does not necessarily require that the Northwind turbines were inactive at the time of recording. Turbines in the Northwind complex are smaller 3 MW Vesta turbines, compared with the larger 7 MW Siemens turbines in the adjacent Rentel wind farm, and therefore they likely generate weaker, higher-frequency vibrations. Similarly, the majority of C-Power wind turbines were not observed, and the one turbine identified (I3) was the weakest observed source. The C-Power Phase-2 6 MW Senvion turbines nearest the cable are installed on steel jacket foundations, while the Rentel turbines are installed with monopile foundations, so some difference in soil-structure interaction is expected.

Discussion and conclusions

The results of this study demonstrate that ambient noise interferometry applied to passive ocean-bottom DAS recordings is a powerful tool for subsurface structural investigation and has the capability of detecting and localizing vibrations from offshore structures. The inverted shear-wave velocity model is generally consistent with the known geologic information. Further, source

images calculated using the measured Scholte wave velocities migrated individual arrivals to within 100 m of known turbine locations. These results were obtained from only about one hour of passive data within the 0.3–4 Hz frequency band. With a longer recording window, the degree of convergence of noise correlation functions (and consequently the signal-to-noise ratio in dispersion images) likely would improve. Similarly, recording at a higher sampling rate would permit utilization of a broader spectrum of environmental noise, such as from short-period microseism and regional shipping traffic, thereby increasing the sensitivity of Scholte wave dispersion spectra to shallow structure and permitting more flexible shear-wave velocity parameterization. However, as in this study, previous passive Scholte wave tomography by Mordret et al. (2013) and de Ridder and Biondi (2013) has been limited to below 2 Hz due to interference from strong, local sources of high-frequency noise. Further work on deblending filters or joint source-structure inversion is needed.

The first proof-of-concept work exploring ocean-bottom DAS deployments was motivated largely by the potential for seismic monitoring in the deep oceans for global tomography or hazard early warning (Lindsey et al., 2019; Sladen et al., 2019; Williams et al., 2019). Today, this vision is not yet practical because (1) subsea cable links are relatively sparse and have not been made widely available to the geoscientific community, and (2) without two-way optical repeaters, commercial DAS systems are limited to less than 100 km operating range. By contrast, application of ocean-bottom DAS for offshore engineering is feasible today because (1) optical fibers are available in power cable networks at existing wind farms, monitoring arrays at subsea oil and gas fields, or along seafloor pipelines, and (2) energy production and development sites are generally within 100 km of the coast or have an associated platform/substation. Further, due to shipping and fishing hazards, ocean-bottom cables in the near-shore environment can include dense armor cladding and are more often buried than deep-sea cables, which is likely to both enhance elastic coupling to the seafloor and reduce temperature-noise in DAS.

Particularly for global wind energy development, deploying DAS on preexisting optical fibers in power cable links has the potential to become a mainstay of offshore engineering practice. For example, shallow gas presents a hazard to drilling operations and foundation integrity. Near the study area on the Belgian Continental Shelf, gas has been identified in Holocene sediments using high-resolution seismic reflection profiles (Missiaen et al., 2002). Because gas concentration has a large impact on bulk modulus but a small impact on shear modulus and density, shear-wave velocity profiling with Scholte waves complementing conventional seismic investigations permits calculation of V_P/V_S for improved constraints on porosity and pore fluid composition. Similarly, soil-structure interaction models, which are increasingly used in the design of wind turbine foundations, require accurate estimates of the stiffness and strength of shallow sediments (e.g., Lombardi et al., 2013). Shear-wave velocity measured in-situ with ocean-bottom DAS can be incorporated in geologic site classification to choose reference strength parameters, or it can be used directly as a proxy in physics-based soil models (e.g., Shi and Asimaki, 2017). Hydrodynamic loading of wind turbines and other offshore structures is another key parameter in foundation design that is difficult to measure in-situ. In addition to seismic signals, ocean-bottom DAS also records the seafloor pressure perturbation from ocean surface gravity waves, which can not only be related to wave intensity (Lindsey et al., 2019) but also current speed (Williams et al., 2019). Ocean-bottom DAS thereby offers diverse value for site selection and foundation design in a geologically and hydrodynamically complex environment such as that of the Belgian offshore.

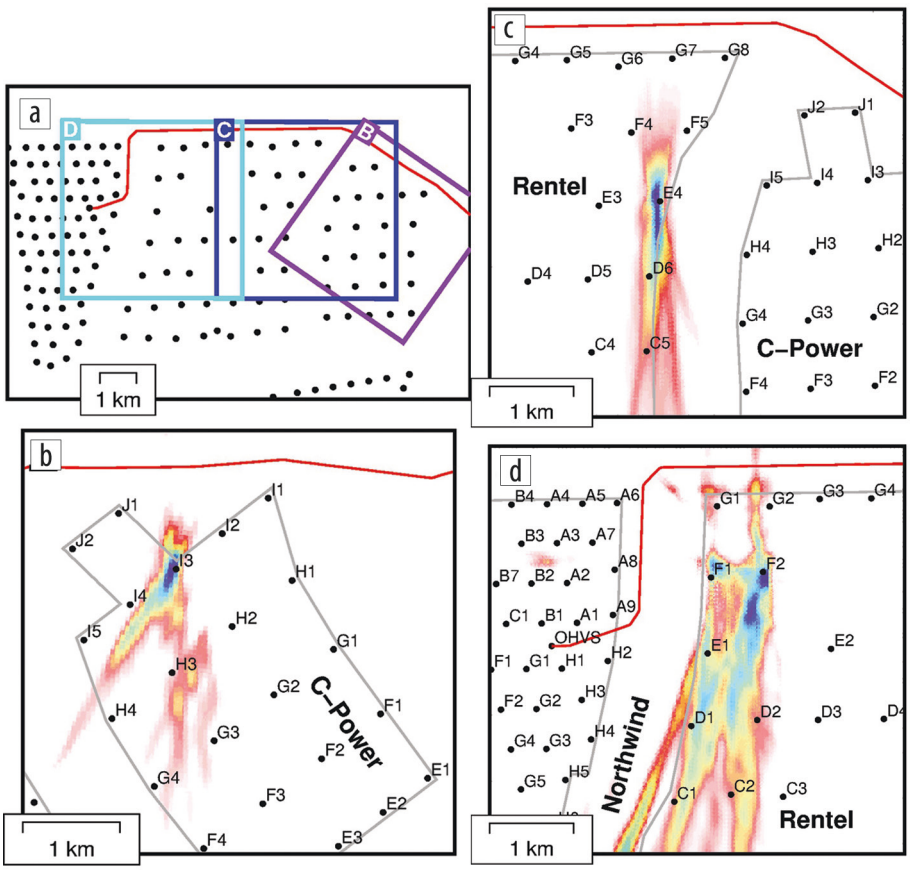

Figure 6. Scholte wave source images. (a) Overview map with locations of three images. The cable location is shown in red, and individual wind turbines are black dots. (b) Source image from common-offset data with midpoints between 29 and 32.5 km showing a single turbine source in the C-Power wind farm. (c) Source image from midpoints 32.5–36.5 km showing a single turbine source in the Rentel wind farm. (d) Source image from midpoints 36.5–41.5 km showing multiple turbine sources in the Rentel wind farm. Each panel has been rotated relative to the local cable orientation, and the color scale is normalized between 0 and 1 in each image.

One major engineering challenge for offshore wind turbines is scouring at the base of the structure, which can jeopardize the integrity of the foundation (Whitehouse et al., 2011). Integration of sediment and water column properties measured with ocean-bottom DAS provides the necessary parameters for scour modeling. Further, our demonstration that ocean-bottom DAS can detect seismic waves radiated from individual wind turbines nearby suggests potential for remote operational and structural health monitoring. Structural vibrations are efficient at generating Scholte waves (or equivalently Rayleigh waves on land) by rocking or shearing of the foundation and Love waves by torsion of the foundation, especially at the natural frequencies of the structure (Favela, 2004). The natural frequencies of wind turbines are highly sensitive to modifications of the sediment-foundation system, such as can be caused by scour (Prendergast et al., 2015). The relative contributions of Scholte and Love waves can also be an indicator of sediment properties and foundation integrity (Favela, 2004). We reserve the development of such methods for future studies where more comprehensive operational ground truth is available.

Presently, the primary limitation of ocean-bottom DAS for engineering applications is the location and timing of cable installation relative to the need for geotechnical information. Preexisting cables will never be installed at the exact site of planned turbines, so ocean-bottom DAS is unlikely to replace in-situ geotechnical coring or cone penetration tests unless dedicated fibers are laid at the design stage. This challenge is partly mitigated in the Belgian offshore by the long history of wind energy development: the first power cable was laid in 2007 with the installation of the C-Power Phase-1 turbines at Thornton Bank, and the cable routes for early installations run through planned development sites (Figure 1). Given the diverse applications of ocean-bottom DAS demonstrated here, offshore wind developers should consider routes that optimize the site selection, design, and monitoring value of seafloor cables for future projects. TLE

Acknowledgments

This work was supported in part by the Comunidad de Madrid and FEDER Program under grant SINFOTON2-CM: P2018/NMT-4326, the European Research Council (OCEAN-DAS: ERC-2019-POC-875302), and the Spanish Government under projects RTI2018–097957-B-C31 and RTI2018–097957-B-C33. E. F. W. was supported by an NSF Graduate Research Fellowship. R. M, M. R. F. R., and H. F. M. acknowledge financial support from the EU's Horizon 2020 research and innovation program (MSCA grant no. 722509EU ITN-FINESSE) and the Spanish MICINN under contracts no. IJC2018–035684-I and IJCI-2017–33856, respectively. Z. Z. acknowledges support from the Moore Foundation and NSF under CAREER Award 1848166.

Data and materials availability

The complete DAS data from this experiment are available on a public data repository at https://doi.org/10.22002/D1.1296.

Corresponding author: efwillia@caltech.edu

References

Abrahamson, N., and W. Silva, 2008, Summary of the Abrahamson and Silva NGA ground-motion relations: Earthquake Spectra, **24**, no. 1, 67–97, https://doi.org/10.1193/1.2924360.

Berryman, J. G., P. A. Berge, and B. P. Bonner, 2002, Estimating rock porosity and fluid saturation using only seismic velocities: Geophysics, **67**, no. 2, 391–404, https://doi.org/10.1190/1.1468599.

Bohlen, T., S. Kugler, G. Klein, and F. Theilen, 2004, 1.5D inversion of lateral variation of Scholte-wave dispersion: Geophysics, **69**, no. 2, 330–344, https://doi.org/10.1190/1.1707052.

Boore, D. M., and W. B. Joyner, 1997, Site amplifications for generic rock sites: Bulletin of the Seismological Society of America, **87**, no. 2, 327–341.

Brocher, T. M., 2008, Compressional and shear-wave velocity versus depth relations for common rock types in northern California: Bulletin of the Seismological Society of America, **98**, no. 2, 950–968, https://doi.org/10.1785/0120060403.

Bryan, G. M., and R. D. Stoll, 1988, The dynamic shear modulus of marine sediments: Journal of the Acoustical Society of America, **83**, 2159–2164, https://doi.org/10.1121/1.396343.

Buckingham, M. J., 2005, Compressional and shear wave properties of marine sediments: Comparisons between theory and data: Journal of the Acoustical Society of America, **117**, 137–152, https://doi.org/10.1121/1.1810231.

Chapman, D. M. F., and O. A. Godin, 2001, Dispersion of interface waves in sediments with power-law shear speed profiles: II. Experimental observations and seismo-acoustic inversions: Journal of the Acoustical Society of America, **110**, 1908–1916, https://doi.org/10.1121/1.1401739.

Cheng, F., B. Chi, N. J. Lindsey, T. C. Dawe, and J. B. Ajo-Franklin, 2021, Utilizing distributed acoustic sensing and ocean bottom fiber optic cables for submarine structural characterization: Scientific Reports, **11**, 5613, https://doi.org/10.1038/s41598-021-84845-y.

Christensen, N. I., and H. F. Wang, 1985, The influence of pore pressure and confining pressure on dynamic elastic properties of Berea sandstone: Geophysics, **50**, no. 2, 207–213, https://doi.org/10.1190/1.1441910.

de Ridder, S. A. L., and B. L. Biondi, 2013, Daily reservoir-scale subsurface monitoring using ambient seismic noise: Geophysical Research Letters, **40**, no. 12, 2969–2974, https://doi.org/10.1002/grl.50594.

de Ridder, S., and J. Dellinger, 2011, Ambient seismic noise eikonal tomography for near-surface imaging at Valhall: The Leading Edge, **30**, no. 5, 506–512, https://doi.org/10.1190/1.3589108.

Dou, S., N. Lindsey, A. M. Wagner, T. M. Daley, B. Freifeld, M. Robertson, J. Peterson, C. Ulrich, E. R. Martin, and J. B. Ajo-Franklin, 2017, Distributed acoustic sensing for seismic monitoring of the near surface: A traffic-noise interferometry case study: Scientific Reports, **7**, 11620, https://doi.org/10.1038/s41598-017-11986-4.

Favela, J., 2004, Energy radiation from a multi-story building: PhD thesis, California Institute of Technology.

Fernandez-Ruiz, M. R., L. Costa, and H. F. Martins, 2019, Distributed acoustic sensing using chirped-pulse phase-sensitive OTDR technology: Sensors, **19**, no. 20, 4368, https://doi.org/10.3390/s19204368.

Fernandez-Ruiz, M. R., H. F. Martins, L. Costa, S. Martin-Lopez, and M. Gonzalez-Herraez, 2018, Steady-sensitivity distributed acoustic sensors: Journal of Lightwave Technology, **36**, no. 23, 5690–5696, https://doi.org/10.1109/JLT.2018.2877849.

Godin, O. A., and D. M. F. Chapman, 1999, Shear-speed gradients and ocean seismo-acoustic noise resonances: Journal of the Acoustical Society of America, **106**, no. 5, 2367–2382, https://doi.org/10.1121/1.428074.

Godin, O. A., and D. M. F. Chapman, 2001, Dispersion of interface waves in sediments with power-law shear speed profiles: I. Exact and approximate analytical results: Journal of the Acoustical Society of America, **110**, no. 4, 1890–1907, https://doi.org/10.1121/1.1401776.

Hamilton, E. L., 1976, Shear-wave velocity versus depth in marine sediments: A review: Geophysics, **41**, no. 5, 985–996, https://doi.org/10.1190/1.1440676.

Hatchell, P. J., P. B. Wills, and C. Didraga, 2009, Production induced effects on near-surface wave velocities at Valhall: 71st Conference and Exhibition, EAGE, Extended Abstracts, https://doi.org/10.3997/2214-4609.201400331.

Jousset, P., T. Reinsch, J. Henninges, H. Blanck, and T. Ryberg, 2017, Crustal exploration and monitoring seismic events with a fibre-optic cable deployed at the ground surface in Iceland: EAGE/DGG Workshop on Fibre Optic Technology in Geophysics, https://doi.org/10.3997/2214-4609.201700169.

Karrenbach, M., R. Ellwood, V. Yartsev, E. Araki, T. Kimura, and H. Matsumoto, 2020, Long-range DAS data acquisition on a submarine fiber-optic cable: EAGE Workshop on Fiber Optic Sensing for Energy Applications in Asia Pacific, https://doi.org/10.3997/2214-4609.202070013.

Le Bot, S., V. Van Lancker, S. Deleu, M. De Batist, J. P. Henriet, and W. Haegeman, 2005, Geological characteristics and geotechnical properties of Eocene and Quaternary deposits on the Belgian continental shelf: Synthesis in the context of offshore wind farming: Netherlands Journal of Geosciences, **84**, no. 2, 147–160, https://doi.org/10.1017/S0016774600023027.

Li, Z., and Z. Zhan, 2018, Pushing the limit of earthquake dtection with distributed acoustic sensing and template matching: A case study at Brady geothermal field: Geophysical Journal International, **215**, no. 3, 1583–1593, https://doi.org/10.1093/gji/ggy359.

Lindsey, N. J., T. C. Dawe, and J. B. Ajo-Franklin, 2019, Illuminating seafloor faults and ocean dynamics with dark fiber distributed acoustic sensing: Science, **366**, no. 6469, 1103–1107, https://doi.org/10.1126/science.aay5881.

Lindsey, N. J., E. R. Martin, D. S. Dreger, B. Freifeld, S. Cole, S. R. James, B. L. Biondi, and J. B. Ajo-Franklin, 2017, Fiber-optic network observations of earthquake wavefields: Geophysical Research Letters, **44**, no. 23, 11792–11799, https://doi.org/10.1002/2017GL075722.

Lombardi, D., S. Bhattacharya, and D. M. Wood, 2013, Dynamic soil-structure interaction of monopile supported wind turbines in cohesive soil: Soil Dynamics and Earthquake Engineering, **49**, 165–180, https://doi.org/10.1016/j.soildyn.2013.01.015.

Ma, Y., R. W. Clayton, V. C. Tsai, and Z. Zhan, 2013, Locating a scatterer in the active volcanic area of Southern Peru from ambient noise cross-correlation: Geophysical Journal International, **192**, no. 3, 1332–1341, https://doi.org/10.1093/gji/ggs103.

Mateeva, A., J. Lopez, J. Mestayer, P. Wills, B. Cox, D. Kiyaschchenko, Z. Yang, W. Berlang, R. Detomo, and S. Grandi, 2013, Distributed acoustic sensing for reservoir monitoring with VSP: The Leading Edge, **32**, no. 10, 1278–1283, https://doi.org/10.1190/tle32101278.1.

Mathys, M., 2009, The quaternary geological evolution of the Belgian Continental Shelf, southern North Sea: PhD thesis, Ghent University.

Missiaen, T., S. Murphy, L. Loncke, and J.-P. Henriet, 2002, Very high-resolution seismic mapping of shallow gas in the Belgian coastal zone: Continental Shelf Research, **22**, no. 16, 2291–2301, https://doi.org/10.1016/S0278-4343(02)00056-0.

Mordret, A., M. Landès, N. M. Shapiro, S. C. Singh, P. Roux, and O. I. Barkved, 2013, Near-surface study at the Valhall oil field from ambient noise surface wave tomography: Geophysical Journal International, **193**, no. 3, 1627–1643, https://doi.org/10.1093/gji/ggt061.

Park, C. B., R. D. Miller, and J. Xia, 1999, Multichannel analysis of surface waves: Geophysics, **64**, no. 3, 800–808, https://doi.org/10.1190/1.1444590.

Park, C. B., R. D. Miller, J. Xia, J. Ivanov, G. V. Sonnichsen, J. A. Hunter, R. L. Good, R. A. Burns, and H. Christian, 2005, Underwater MASW to evaluate stiffness of water-bottom sediments: The Leading Edge, **24**, no. 7, 724–728, https://doi.org/10.1190/1.1993267.

Pastor-Graells, J., H. F. Martins, A. Garcia-Ruiz, S. Martin-Lopez, and M. Gonzalez-Herraez, 2016, Single-shot distributed temperature and strain tracking using direct detection phase-sensitive OTDR with chirped pulse: Optics Express, **24**, no. 12, 13121–13133, https://doi.org/10.1364/OE.24.013121.

Prendergast, L. J., K. Gavin, and P. Doherty, 2015, An investigation into the effect of scour on the natural frequency of an offshore wind turbine: Ocean Engineering, **101**, 1–11, https://doi.org/10.1016/j.oceaneng.2015.04.017.

Schuster, G. T., J. Yu, J. Sheng, and J. Rickett, 2004, Interferometric/daylight seismic imaging: Geophysical Journal International, **157**, no. 2, 838–852, https://doi.org/10.1111/j.1365-246X.2004.02251.x.

Seed, H. B., and I. M. Idriss, 1970, Soil moduli and damping factors for dynamic response analyses: Technical report, UCB/EERC-70/10, Earthquake Engineering Research Center, University of California at Berkeley.

Shapiro, N. M., M. Campillo, L. Stehly, and M. H. Ritzwoller, 2005, High-resolution surface-wave tomography from ambient seismic noise: Science, **307**, no. 5715, 1615–1618, https://doi.org/10.1126/science.1108339.

Shi, J., and D. Asimaki, 2017, From stiffness to strength: Formulation and validation of a hybrid hyperbolic nonlinear soil model for site-response analyses: Bulletin of the Seismological Society of America, **107**, no. 3, 1336–1355, https://doi.org/10.1785/0120150287.

Sladen, A., D. Rivet, J. P. Ampuero, L. De Barros, Y. Hello, G. Calbris, and P. Lamare, 2019, Distributed sensing of earthquakes and ocean-solid earth interactions on seafloor telecom cables: Nature Communications: **10**, 5777, https://doi.org/10.1038/s41467-019-13793-z.

Spica, Z. J., K. Nishida, T. Akuhara, F. Petrelis, M. Shinohara, and T. Yamada, 2020a, Marine sediment characterized by ocean-bottom fiber-optic seismology: Geophysical Research Letters, **47**, no. 16, https://doi.org/10.1029/2020GL088360.

Spica, Z. J., M. Perton, E. R. Martin, G. Beroza, and B. Biondi, 2020b, Urban seismic site characterization by fiber-optic seismology: Journal of Geophysical Research: Solid Earth, **125**, no. 3, https://doi.org/10.1029/2019JB018656.

Tanimola, F., and D. Hill, 2009, Distributed fibre optic sensors for pipeline protection: Journal of Natural Gas Science and Engineering, **1**, no. 4–5, 134–143, https://doi.org/10.1016/j.jngse.2009.08.002.

Tsai, V. C., and S. Atiganyanun, 2014, Green's functions for surface waves in a generic velocity structure: Bulletin of the Seismological Society of America, **104**, no. 5, 2573–2578, https://doi.org/10.1785/0120140121.

Wang, X., E. F. Williams, M. Karrenbach, M. Gonzalez-Herraez, H. F. Martins, and Z. Zhan, 2020, Rose parade seismology: Signatures of floats and bands on optical fiber: Seismological Research Letters, **91**, no. 4, 2395–2398, https://doi.org/10.1785/0220200091.

Whitehouse, R. J. S., J. M. Harris, J. Sutherland, and J. Rees, 2011, The nature of scour development and scour protection at offshore windfarm foundations: Marine Pollution Bulletin, **62**, 73–88, https://doi.org/10.1016/j.marpolbul.2010.09.007.

Williams, E. F., M. R. Fernández-Ruiz, R. Magalhaes, R. Vanthillo, Z. Zhan, M. González-Herráez, and H. F. Martins, 2019, Distributed sensing of microseisms and teleseisms with submarine dark fibers: Nature Communications, **10**, 5778, https://doi.org/10.1038/s41467-019-13262-7.

Zeng, X., C. Lancelle, C. Thurber, D. Fratta, H. F. Wang, N. Lord, A. Chalari, and A. Clarke, 2017, Properties of noise cross-correlation functions obtained from a distributed acoustic sensing array at Garner Valley, California: Bulletin of the Seismological Society of America, **107**, no. 2, 603–610, https://doi.org/10.1785/0120160168.

Zhan, G., J. P. van Gestel, and R. Johnston, 2020, DAS data recorded by a subsea ubilical cable at Atlantis field: 90th Annual International Meeting, SEG, Expanded Abstracts, 510–514, https://doi.org/10.1190/segam2020-3427669.1.

Zhan, Z., 2020, Distributed acoustic sensing turns fiber-optic cables into sensitive seismic antennas: Seismological Research Letters, **91**, no. 1, 1–15, https://doi.org/10.1785/0220190112.

Zhan, Z., S. Ni, D. V. Helmberger, and R. W. Clayton, 2010, Retrieval of Moho-reflected shear wave arrivals from ambient seismic noise: Geophysical Journal International, **182**, no. 1, 408-420, https://doi.org/10.1111/j.1365-246X.2010.04625.x.